

Numerical Investigation Into the Simultaneous Growth of Two Closely Spaced Fluid-Driven Fractures

XiYu Chen, Southwest Petroleum University, China; Monash University, Australia; and CSIRO Energy;
Jinzhou Zhao, Southwest Petroleum University, China; **Wenyi Yan**, Monash University, Australia;
and **Xi Zhang**, CSIRO Energy

Summary

Multistage, multicluster hydraulic fracturing is a widespread method used in the petroleum industry to enhance the hydrocarbon production of low-permeability unconventional reservoirs. The core for fracturing-treatment success is achieving the simultaneous propagation of multiple closely spaced hydraulic fractures to enlarge the fracture surface. To better understand this coupled elasto-hydrodynamics mechanics, a 2D model comprising a combination of a displacement discontinuity method for elasticity and a finite volume method for lubrication is presented in this paper. Furthermore, a universal tip asymptotic solution, reflecting the unique multiscale tip behavior for fluid-driven fractures, is adopted as a propagation criterion to locate the fracture front. Numerical examples are fully implemented to investigate the competition in the growth of two closely spaced fluid-driven fractures at different initial lengths. Parametric studies reveal that the competition between simultaneous and single fracture growth is governed by dimensionless toughness, which represents the energy ratio of fracture-surface creation to fluid viscous dissipation. The simultaneous growth will be promoted when the fluid viscous dissipation is dominant, while, with increasing rock toughness, the tendency for single-fracture growth will increase correspondingly. Numerical results also demonstrate that initial fracture geometric settings play an important role in this competition. A large initial length offset between two fractures will generate preferential growth for the longer fracture, even in the viscosity-dominated regime. Furthermore, this paper provides dimensionless parameters characterizing fracture deflection caused by fracture interaction. The paper concludes by identifying the controlling parameters and their field applications, emphasizing that high injection rate, high fluid viscosity, and small initial fracture-size offset are beneficial to promoting the simultaneous growth at early time, which is important in enhancing reservoir permeability.

Introduction

Fluid-driven fractures (hydraulic fractures) are induced by the injection of pressurized fluid into a solid medium. They exhibit, in nature, as magmatic dikes that propagate upward from underground chambers driven by buoyancy (Spence et al. 1987; Rubin 1995; Roper and Lister 2005), thin sheet-like magma bodies that intrude into the existing bedding planes (Pollard and Holzhausen 1979; Spence and Sharp 1985; Bunger and Cruden 2011), and fractures at glacier beds associated with turbulent flow (Tsai and Rice 2010). In the petroleum industry, artificial hydraulic fracturing is widely used to enhance recovery by pumping viscous fluid into rock (Economides et al. 2000). These man-made fractures propagate in rock subjected to in-situ compressive stress and eventually become highly permeable migration pathways for hydrocarbon. In addition, the hydraulic-fracturing technique is also applied to preconditioning rock for block-caving mining (Jeffrey et al. 2013), waste disposal (Bell 2004), and enhanced geothermal systems (Legarth et al. 2005).

In recent years, the multistage and multicluster hydraulic-fracturing technique has become one of the most widespread methods to enhance the hydrocarbon production of low-permeability unconventional reservoirs in the petroleum industry (King 2010). With smaller perforation intervals and more proppants, multiple closely spaced fluid-driven fractures are claimed to have enhanced production rates (**Fig. 1**). However, the formation of closely spaced fractures by the aggressive treatment has not been justified. Production-log data indicate that a considerable part of perforation clusters are nonproductive after the multistage hydraulic-fracturing treatment (Miller et al. 2011), which implies the failure of simultaneous fracture growth. Fiber-optic diagnostic data more clearly show that the significantly uneven growth of multiple fractures often occurs because only a small number of the fractures preferentially take most of the injected fluid (Ugueto et al. 2016; Somanchi et al. 2016). This preferential-growth phenomenon introduces doubt about the effectiveness of the aggressive fracturing treatments. With increasing attention to the growth competition between multiple fluid-driven fractures, many field investigations and numerical studies performed in the past 10 years have found that a strong stress interaction is a key cause in impeding the simultaneous multifracture growth (e.g., Fisher et al. 2004; Germanovich and Astakhov 2004; East et al. 2011; Meyer and Bazan 2011; Nagel and Sanchez-Nagel 2011). Numerical studies show that the fracture interactions will reduce the fracture widths, rapidly readjust the fluid-influx partition, and result in a preferential-growth mode, which is consistent with fiber-optic diagnostic data in practice (e.g., Olson 2008; Roussel and Sharma 2011; Wu and Olson 2015; Lecampion and Desroches 2015b; Zhao et al. 2016). As such, the hydraulic fractures are often localized in a few fracture paths.

In nature, dike swarms normally have a relatively high length/spacing ratio. It is curious that these natural fluid-driven dikes can propagate together instead of focusing, possibly from one source (**Fig. 2**). It is intuitive that there is competition between two fracture-growth modes: simultaneous and preferential growth. To investigate this competition mechanism, Zhang and Jeffrey (2012) and Zhang et al. (2014) focused on the growth and interaction of closely spaced hydraulic fractures in the natural stress and rheology environments by investigating two magmatic fractures driven by more-viscous fluids using a fully coupled 2D model. These studies revealed that the simultaneous growth of the fluid-driven fracture at a low separation is energetically favorable compared with the single-fracture growth. The promotion of simultaneous growth is a consequence of fluid/solid coupling in which fluid viscous dissipation plays a vital role. From the point of view of input power, Bunger (2013) has calculated the energy required to simultaneously propagate multiple hydraulic fractures, and he concluded that simultaneous growth seems to be more stable in a viscosity-dominated regime. From energy

analysis, he predicted that, in a toughness-dominated regime, by contrast, fewer growing hydraulic fractures will be produced because suppressed fractures can reach only much shorter lengths than in the viscosity-dominated regime. Fluid viscous dissipation may act as an impetus for a simultaneous-fracture-growth mode; however, so far, how it works is still unclear. Whether this mechanics can be properly used to create denser, closely spaced fractures to optimize multistage hydraulic fracturing is becoming a popular subject in petroleum-industry research (e.g., Bunger et al. 2014; Peirce and Bunger 2015; Bunger and Lecampion 2017). The main goal of this paper, therefore, is to use a numerical model with an iteratively coupled algorithm to seek the conditions that favor fluid-driven fractures to simultaneously grow to a reasonable distance and to quantify the growth extents no matter which fracture-growth mode is dominant.

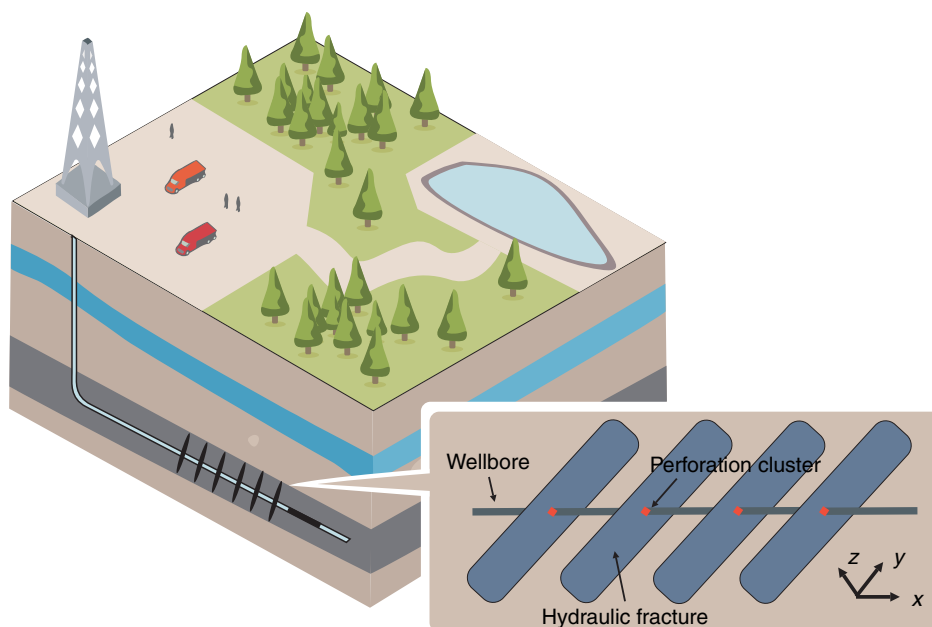


Fig. 1—Schematic of multistage and multicluster hydraulic fracturing in the petroleum industry.

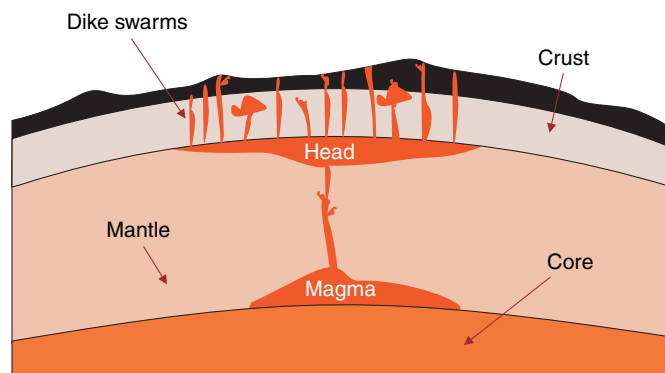


Fig. 2—Natural closely spaced hydraulic fractures—dike swarms.

In this paper, we first present a coupled 2D numerical model for simulating the simultaneous growth of fluid-driven fractures. To solve this elasto-hydrodynamics problem, a combination of the displacement discontinuity method for elasticity and the finite volume method for lubrication is used. We adopt a universal tip asymptotic solution in this model as the propagation criterion to locate the fracture front. One advantage is that our model thus can properly capture the unique multiscale tip behavior for fluid-driven fracture growth, so that it can cope with the viscosity-to-toughness transition regime to a large degree. In the next section, we compare our numerical results with published analytical solutions to verify our model. Then, we choose numerical examples to investigate the competition in the growth of two closely spaced fluid-driven fractures at different initial lengths. Parametric studies on scaling arguments are conducted to clarify the fracture-interaction mechanisms and to identify the governing parameters for simultaneous vs. preferential fracture growth. Meanwhile, the dimensionless parameter characterizing fracture deflection is also calibrated in a quantitative manner. Finally, we discuss some field implications on the basis of the results of our parametric studies and provide guidance for fracturing-treatment design.

Numerical Model

Assumptions. In this study, we developed a 2D numerical model modified from our previous study (Zhao et al. 2017) to simulate the simultaneous propagation of two fluid-driven fractures. This coupled 2D model can cope with nonplanar multiple-fracture propagation with a high numerical efficiency. Although the 2D model cannot capture the realistic fracture surface, it can render more direct results

to reveal the mechanisms associated with simultaneous fracture growth, as did most other models (Sesetty and Ghassemi 2016; Wu et al. 2017; Zeng et al. 2018).

Assumptions adopted in this model include

- The reservoir rock is elastic and impermeable. The effect of poroelasticity on hydraulic fracturing is not considered in the model, although it is important for some cases. The Young's modulus E , Poisson's ratio ν , and fracture toughness K_{IC} are uniform across the infinite medium.
- The fluid-driven fracture propagation (mixed I/II Mode) obeys the theory of linear elastic-fracture mechanics (LEFM), and the propagation direction follows the maximum hoop-stress criterion (Erdogan and Sih 1963).
- The injection fluid is assumed to be an incompressible Newtonian fluid.
- Fluid-driven fractures are fully filled by the injection fluid. In other words, there is no lag between the fracture front and fluid front. In fact, the lag is typically negligible in deep conditions (Detournay 2016), so the no-lag assumption is acceptable.
- No limited-entry method is present, and the fluid-pressure drop caused by perforation friction is negligible. A high pressure drop caused by perforation friction can balance the influx rates of fractures and promote simultaneous fracture growth to some extent, and the technology using this impetus is the so-called limited-entry method (Daneshy 2015; Lecampion and Desroches 2015b; Wu and Olson 2015). However, the goal of this paper is to investigate the potential fracture-interaction mechanism for promoting simultaneous growth, as mentioned in the Introduction, without the assistance of perforation friction or other placed devices. Thus, a negligible pressure drop caused by perforation friction is adopted in our model to avoid its interference on the following analysis.

One should remember that our study focuses on multistage hydraulic fracturing, which is widely used in very-low-permeability unconventional reservoirs such as a shale gas reservoir or a tight gas reservoir (typical permeability $k \ll 0.1$ md). In such situations, the rock is highly impermeable, and the fluid leakoff has little effect on the fracture-propagation process. For this reason, the previous assumption is acceptable. If the permeability is not low (e.g., rock permeability $k \gg 0.1$ md), the numerical model presented next can be extended by introducing a Carter leakoff model (Howard and Fast 1957), which will increase the calculation time and is not necessary for this study.

Governing Equations. In the following subsections, we will discuss the governing equations for the problem shown in Fig. 3. Two closely spaced initial fractures are placed parallel at different initial lengths. The initial half-lengths of short and long fractures are denoted as l_1 and l_2 . The initial spacing between the two fractures is denoted as D . Two fractures are driven by a constant fluid injection from the wellbore. This study targets only the relatively early stage of fracture propagation, when hydraulic fractures are well-confined within the pay zone because of the layer structure of the unconventional reservoir. Thus, the fracture heights H are equal to the thickness of the pay zone. Under the internal pressure, the leading edge of the hydraulic fracture is flat, on the basis of the fracture-pattern stability analysis by Rice (1985). Then, two fractures are characterized by two initial half-lengths as shown in Fig. 3. In this fluid-driven fracture-growth problem, the time histories of fracture opening $w(x,y,t)$, fracture-surface shear displacement $v(x,y,t)$, fluid pressure $p(x,y,t)$, and fracture-propagation footprint $S(x,y,t)$ are governed by a set of equations that are based on linear elastic deformation, fluid lubrication, fluid mass conservation, propagation criterion, and boundary conditions. To solve this time-dependent problem, the reservoir-rock properties (Young's modulus E , Poisson's ratio ν , and rock toughness K_{IC}), the far-field stress ($\sigma_{c,max}$ and $\sigma_{c,min}$), injection rate Q , and fracturing-fluid viscosity μ are input parameters. For simplicity, three combined parameters (E' , μ' , K') are used in the following:

$$E' = \frac{E}{1-\nu^2}, \quad \mu' = 12\mu, \quad K_I' = 4\left(\frac{2}{\pi}\right)^{1/2} K_{IC}. \quad (1)$$

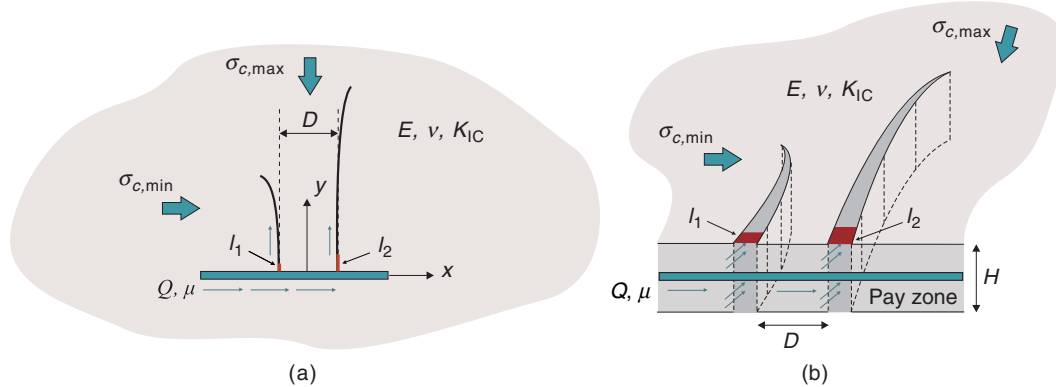


Fig. 3—Schematics of simultaneous growth of two closely spaced fluid-driven fractures. Fracture height is fixed as H : (a) plan view and (b) 3D view. Because of the symmetry, only the upper half is illustrated in this figure.

Elasticity. As shown in Fig. 3, we assume that the well is oriented in the direction of the minimum horizontal in-situ stress (x -direction) and that initial fractures are transverse to the well (y -direction). Note that the more compressive it is, the larger the stress. Given the coordinates, the relation between the fracture opening w , shear displacement v , and the fluid pressure p within the fracture footprint S can be written as boundary integral equations (Crouch and Starfield 1983),

$$\begin{aligned} p(x,y) - \sigma_c^n &= \int_S [c_{nn}w(x_0,y_0) + c_{ns}v(x_0,y_0)]ds; \\ -\sigma_c^s &= \int_S [c_{sn}w(x_0,y_0) + c_{ss}v(x_0,y_0)]ds, \end{aligned} \quad (2)$$

where the indices n and s mean the normal and shear directions. The hypersingular Green's functions c_{nn} , c_{ns} , c_{sn} , and c_{ss} are the influence functions to represent stress components at point (x,y) caused by displacement discontinuity components at the fracture surface (x_0,y_0) .

Mixed-Mode Fracture Propagation. On the basis of the LEFM, the Mode I fracture will propagate when the stress-intensity factor reaches the fracture toughness. The stress-intensity factor at the fracture tip, moving in equilibrium in light of the fracture toughness, is given by

$$\lim_{r \rightarrow 0} \frac{w}{r^{1/2}} = \frac{K_I'}{E'}, \quad \dots \quad (3)$$

where r is the distance to the fracture tip.

The LEFM-based propagation criterion (Eq. 3) represents a relation of the fracture opening w with the distance from the fracture tip r and, thus, it can be applied to locate the position of the fracture tip in the numerical model. However, this propagation criterion (Eq. 3) is typically valid in a small zone close to the fracture tip due to the multiscale tip behavior of the hydraulic fracture (Appendix B). To use such a propagation criterion, very fine meshes should be adopted in the tip zone, which will significantly impair the computational efficiency of the numerical model. Thus, instead of using the propagation criterion of Eq. 3, in this model an approximately universal asymptotic solution (Dontsov and Peirce 2015) is adopted as the propagation criterion,

$$\lim_{r \rightarrow 0} w = \left(\frac{K_I'^3}{E'^3} r^{\frac{3}{2}} + 2 \cdot 3^{\frac{5}{2}} \frac{\mu' V r^2}{E'} \right)^{\frac{1}{3}}, \quad \dots \quad (4)$$

where $V = (r - r_o)/\Delta t$ is the propagation velocity and r, r_o are distances from a specified point to the tip at the current timestep and the last timestep. This asymptotic solution effectively reflects the unique multiscale tip behavior for fluid-driven fractures. In the cases of $\mu' = 0$ or $K_I' = 0$, the asymptotic solution (Eq. 4) will degenerate to two limiting solutions in a toughness-dominated regime and a viscosity-dominated regime, respectively, as (Detournay 2004)

$$w_k = \frac{K_I'}{E'} r^{\frac{1}{2}}, \quad w_m = 2^{\frac{1}{3}} 3^{\frac{5}{6}} \left(\frac{\mu' V}{E'} \right)^{\frac{1}{3}} r^{\frac{2}{3}}, \quad \dots \quad (5)$$

In multiple fluid-driven fracture growth, fracture-propagation paths can deflect, depending on the mixed I/II Mode loading conditions. For this reason, in this paper, the previous universal asymptotic solution (Eq. 4) is modified further for mixed I/II Mode, on the basis of the maximum-hoop-stress criterion (Erdogan and Sih 1963). The local fracture-deflection angle θ during fracture growth is dependent on the ratio $\kappa = K_{II}/K_I$. The θ and κ can be calculated by

$$\tan(\theta/2) = -\frac{2\kappa}{1 + \sqrt{1 + 8\kappa^2}}, \quad \kappa = \lim_{r \rightarrow 0} \frac{v}{w}. \quad \dots \quad (6)$$

By introducing the maximum-hoop-stress criterion (Erdogan and Sih 1963) to calculate the maximum opening along the deflection angle, Eq. 4 is rewritten as

$$\cos \frac{\theta}{2} \left(\cos^2 \frac{\theta}{2} \lim_{r \rightarrow 0} w - \frac{3}{2} \sin \theta \lim_{r \rightarrow 0} v \right) = \left[\frac{K_I'^3}{E'^3} r^{\frac{3}{2}} + 2 \cdot 3^{\frac{5}{2}} \frac{\mu' (r - r_o) r^2}{\Delta t E'} \right]^{\frac{1}{3}}. \quad \dots \quad (7)$$

Lubrication. Newtonian fluid flow in a fracture is controlled by Poiseuille's law,

$$q = -\frac{w^3}{\mu'} \nabla p, \quad \dots \quad (8)$$

where $\nabla = (\partial/\partial l)$ is the gradient operator along the fracture footprint. The continuity of mass balance for the incompressible fluid can be expressed as

$$\frac{\partial w}{\partial t} + \nabla q = Q \delta(0), \quad \dots \quad (9)$$

where the Dirac delta function δ is used to represent the point sources of an injection array.

Boundary Conditions. Although the total injection rate Q is a known parameter, its partition into each fracture is undetermined. The i th fracture growing along the footprint $S_i(t)$, is driven by the i th influx rate $q_i(t)$ at the inlet point $(0, y_i)$. When neglecting the pressure drops caused by wellbore friction and perforation friction, the fluid pressure p_i^{inlet} should be the same at the two fracture inlets, and hence, the influx rate $q_i(t)$ for each inlet is adjusted accordingly. In addition, the sum of the influx rates injected into two fractures is equal to the injection rate Q . The previous constraint conditions can thus be expressed as

$$\begin{cases} Q = \sum_{i=1}^{N=2} q_i \\ p_1^{\text{inlet}} = p_2^{\text{inlet}}, \end{cases} \quad \dots \quad (10)$$

in which the fracture-inlet pressure p^{inlet} can be obtained by solving the elasto-hydrodynamics coupling equation. The derivation of the conditions expressed in Eq. 10 is presented in Appendix C.

To close the formulated problem, proper boundary conditions at the fracture tip are also required. The zero-opening boundary condition and the zero-flux boundary condition at fracture fronts are expressed as

$$\lim_{r \rightarrow 0} w = 0, \quad \lim_{r \rightarrow 0} q = 0. \quad \dots \quad (11)$$

Numerical Scheme. A combination of the displacement discontinuity method for elasticity and the finite volume method for lubrication is used to solve the elasto-hydrodynamics coupling problem. A detailed description of the numerical scheme for finding the solutions is presented in Appendix A and in the previous study (Zhao et al. 2017). In this numerical model, a simple version of the implicit

level-set algorithm originally proposed for planar 3D hydraulic-fracture growth (Peirce and Detournay 2008) is also used to assist in locating the fracture-tip position. However, some modifications are made in this algorithm for the case of nonplanar fracture growth. As shown in Fig. 4, the fracture elements are divided into two types on the basis of their positions: tip elements and channel elements. The channel element next to the tip element is defined as the survey element indicated by red color in Fig. 4. In each iteration, an updated fracture opening w and a shear displacement v at the survey element are adopted to calculate the local deflection angle θ . Also, the updated w and v at the survey element are used to calculate the distance r from the center of the survey element to the fracture tip using the asymptotic relation (Eq. 7). After obtaining both θ and r , the fracture tip is updated to the new position. This iteration will be repeated until the convergence of the tip position is reached. To make the numerical scheme clear to readers, the flow chart of our numerical method is provided in Table 1.

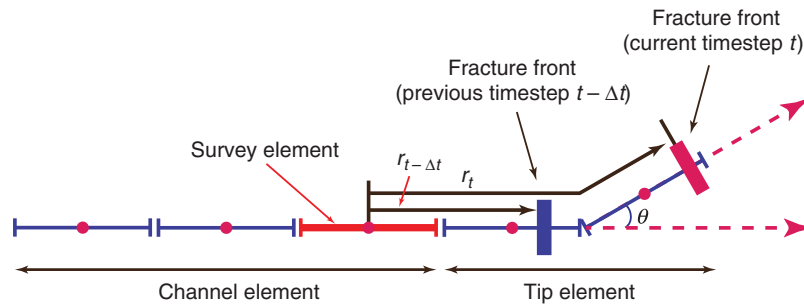


Fig. 4—Fracture elements in the numerical model. The elements are classified as channel elements and tip elements. The current tip element varies in both length and deflection angle.

```

1: Set initial conditions
2: while Total time is not arrived do
3:   while Fracture-tip position is not converged do
4:     while Condition (10) is not reached do
5:       Solve elasto-hydrodynamics coupling for new  $w$ ,  $v$ , and  $p$ 
6:       Use iteration to adjust influx rate  $q$ 
7:     end while
8:     Calculate  $\theta$  with updated  $v$  and  $w$ 
9:     Calculate  $r$  based on updated  $w$ ,  $v$ , and  $\theta$ 
10:    Update fracture-tip position with new  $r$  and  $\theta$ 
11:  end while
12:   $t = t + \Delta t$ 
13: end while

```

Table 1—Numerical method flow chart.

Numerical Simulations and Results

Scaling. Many input parameters govern this fluid-driven fracture-growth problem, as mentioned in the Governing Equations subsection. Thus, a complete parametric analysis using these original parameters such as E' , μ' , K' , Q , σ_c will be tedious and time-consuming. Furthermore, such extensive analyses still cannot clearly capture the full relationship between these parameters and physical mechanisms. By contrast, dimensional analysis and proper scaling are applied here to significantly reduce the efforts of parametric analysis by considering fewer dimensionless parameter groups. More importantly, parametric analysis using dimensionless parameters can obtain deeper insights to clarify the intrinsic mechanism. In the following, we first scale these parameters into dimensionless forms to better perform the subsequent analysis.

In the case of propagating the fluid-driven fracture with constant injection rate Q , following the viscosity scaling given by Detournay (2004), the rock toughness can be scaled as

$$K' = \varepsilon E' \zeta^{1/2} \mathcal{K}, \quad \dots \dots \dots (12)$$

where ε and ζ are a dimensionless small number and a length scale, respectively, defined by

$$\varepsilon = \left(\frac{\mu'}{E't} \right)^{1/3}, \quad \zeta = \left(\frac{E'Q^3 t^4}{\mu'} \right)^{1/6} \dots \dots \dots (13)$$

Then, the dimensionless toughness \mathcal{K} is expressed as

$$\mathcal{K} = \frac{K'}{(E'^3 \mu' Q)^{1/4}} \dots \dots \dots (14)$$

Dimensionless toughness \mathcal{K} represents the energy ratio of a fracture-surface creation to viscous dissipation (Detournay 2004). It quantitatively characterizes the fracture-propagation regime according to which process dominantly consumes the input energy and controls the fracture propagation. In the case of $\mathcal{K} < 1$, the propagation regime is viscosity-dominated, and the rock toughness has no significant effect on fracture propagation. Then, the solution of the fracture-growth problem is approximately equal to the M -solution ($K' = 0$) (Detournay 2004). In contrast, the regime is toughness-dominated when $\mathcal{K} > 4$, and the solution can be approximated by the K -solution (no fluid viscosity because $\mu' = 0$) accordingly. The propagation regime is called the transition regime when $1 \leq \mathcal{K} \leq 4$, and within it, two energy-dissipation processes are involved together.

In the case of growth of two closely spaced fractures, the induced stress between fractures can be scaled by $(E'^3 \mu' Q)^{1/4} / \sqrt{D}$ or K' / \sqrt{D} , depending on the dominant regime. In addition, the far-field differential stress $\Delta\sigma = \sigma_{c,\max} - \sigma_{c,\min}$ also can be scaled by $(E'^3 \mu' Q)^{1/4} / \sqrt{D}$ and K' / \sqrt{D} for the two extreme regimes, respectively. The dimensionless differential stress χ was previously used by Bungier et al. (2012) as

$$\chi_m = \frac{\Delta\sigma\sqrt{D}}{(E'^3 \mu' Q)^{1/4}}, \quad \chi_k = \frac{\Delta\sigma\sqrt{D}}{K'}. \quad (15)$$

Obviously, the dimensionless parameter χ is related to the fracture deflection during propagation because it captures the intrinsic mechanism that the path curving caused by induced stress is suppressed by the constraint of far-field differential stress.

The coordinates x , y and fracture initial half-lengths l are scaled by fracture spacing D . Also, a ratio of initial half-lengths is introduced as ρ . They are given as

$$x' = \frac{x}{D}, \quad y' = \frac{y}{D}, \quad \eta = \frac{l_2}{D}, \quad \rho = \frac{l_1}{l_2}. \quad (16)$$

In the following parametric analysis, all numerical examples are performed up to the time when a fracture half-length in the presence of a single fracture, without fracture interaction, can reach twice the fracture spacing D under a constant-injection flow rate Q . This arrangement can ensure that, in all numerical cases, a same-level fluid volume will be considered no matter how distinct the parameters are. Meanwhile, the given input volume is typically not too large for accomplishing the competitive growing process of two fractures.

Because this study focuses mainly on the mechanism of fracture-growth competition, we will limit our study scope to the fracture footprints S and influx partition. To present the growth-competition results, we introduce two coefficients of variation $C_{v,l}$ and $C_{v,q}$, which are standardized measures of half-length and influxes between two fractures:

$$C_{v,l} = \frac{\varsigma_l}{\bar{l}}, \quad C_{v,q} = \frac{\varsigma_v}{\bar{V}_q}, \quad (17)$$

in which ς_l and ς_v are standard deviations for half-lengths and influxes of two fractures, and \bar{l} and \bar{V}_q are mean values for half-lengths and influxes of two fractures.

The dimensionless parameters $C_{v,l}$ and $C_{v,q}$ are able to quantitatively represent the competition in the growth of the two fractures. The low coefficient of variation means a relatively simultaneous growth of two fractures with similar fracture lengths and fluid volumes. On the contrary, a higher coefficient of variation indicates preferential growth.

By introducing the previous dimensionless parameters, the study finds the functional relations as

$$[C_{v,l}, C_{v,q}, S(x', y')] = f(\mathcal{K}, \chi, \rho, \eta). \quad (18)$$

Then the parametric analysis for this problem can be performed by varying only four dimensionless parameters (\mathcal{K} , χ , ρ , η) associated with energy dissipation (\mathcal{K}), fracture deflection ($\chi = \chi_m$ or χ_k), and initial fracture geometric settings (ρ, η).

Model Validation. Before starting the parametric analysis, a validation study is performed to verify our numerical model. In **Fig. 5**, we compare our numerical results of single-fracture growth with published analytical solutions (Adachi 2001; Detournay 2004; Adachi and Detournay 2008) in different conditions (listed in **Table 2**) corresponding, respectively, to the viscosity-dominated regime, the transition regime, and the toughness-dominated regime. As **Fig. 5** shows, in the cases of $\mathcal{K} = 0.0365$ (viscosity-dominated) and $\mathcal{K} = 4.1824$ (toughness-dominated), numerical results of half-length and inlet pressure are well consistent with the analytical M -solution and K -solution accordingly. In addition, in the case of $\mathcal{K} = 2.1928$ ($1 \leq \mathcal{K} \leq 4$), our transition-regime solution is compared with published solutions for $\mathcal{K} = 2$ and $\mathcal{K} = 3$ provided by Adachi (2001). As shown in **Fig. 5b**, the numerical result for $\mathcal{K} = 2.1928$ lies between these two solutions and approaches the smaller \mathcal{K} solution. By adopting the universal asymptotic-tip solution (Eq. 7), this model can also effectively deal with the fracture-propagation problem in the transition regime. Therefore, our model can reasonably provide acceptable results for an arbitrary value of \mathcal{K} , which is critical for our following parametric analyses.

The Influence of Dimensionless Toughness \mathcal{K} . In this subsection, we first investigate how the propagation regime, namely dimensionless toughness \mathcal{K} , affects the growth competition of two closely spaced fractures. In total, 42 numerical examples are performed with fixed $\rho = 0.8$, $\eta = 0.08$ but varying \mathcal{K} . In the base numerical example, the physical parameters are $E = 3.5 \times 10^4$ MPa, $\nu = 0.2$, $\mu = 10^{-8}$ MPa \cdot s, $Q = 0.001$ m²/s, $\Delta\sigma = 2$ MPa and $K_{IC} = 1$ MPa \cdot m^{0.5}. To vary \mathcal{K} in the rest of the 41 numerical examples, one or two parameters will be changed while remaining parameters are maintained to the base values.

The values of $C_{v,l}$ and $C_{v,q}$ for each of the 42 numerical examples are shown in **Fig. 6**. First, it can be found that both coefficients of variation $C_{v,l}$ and $C_{v,q}$ with varying \mathcal{K} show a similar varying trend. All the simulation results are located around an S-type curve, which indicates that the dimensionless toughness \mathcal{K} effectively governs the growth competition of closely spaced fractures. As shown in **Fig. 6**, a similar \mathcal{K} will generate a similar growth-competition result. Second, the curves of $C_{v,l}$ and $C_{v,q}$ show an upsurge when the dimensionless toughness \mathcal{K} is close to 1.0, which is the boundary between the viscosity-dominated and transition regimes. A nearly simultaneous growth pattern, indicated by lower coefficients of variation, can be obtained only when $\mathcal{K} < 1$ (in the viscosity-dominated regime). With increasing \mathcal{K} , the tendency toward a single-fracture growth becomes more obvious.

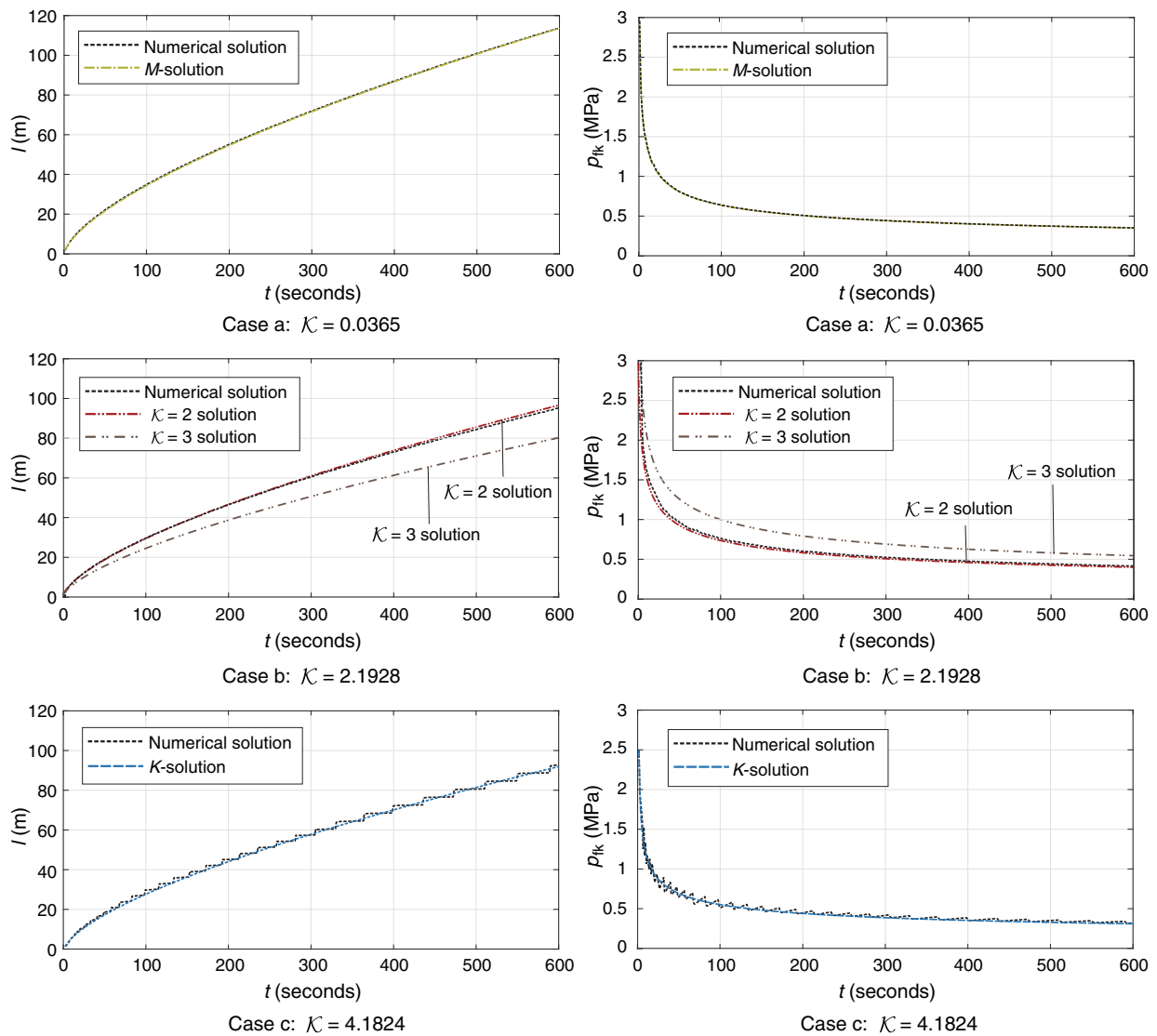


Fig. 5—Validation cases (a through c). The results of half-length l and inlet pressure p_{ik} are compared with the solutions presented by Adachi (2001); Detournay (2004); and Adachi and Detournay (2008).

Cases	E (MPa)	ν	μ (mPa·s)	K_{IC} (MPa·m ^{0.5})	Q (m ² /s)	\mathcal{K}	Regime
a	35 000	0.2	10	0.1	0.001	0.0365	Viscosity
b	35 000	0.2	10	6	0.001	2.1928	Transition
c	25 000	0.2	1	5	0.001	4.1824	Toughness

Table 2—Parameters for validation cases. Cases a, b, and c correspond to viscosity, transition, and toughness regimes, respectively.

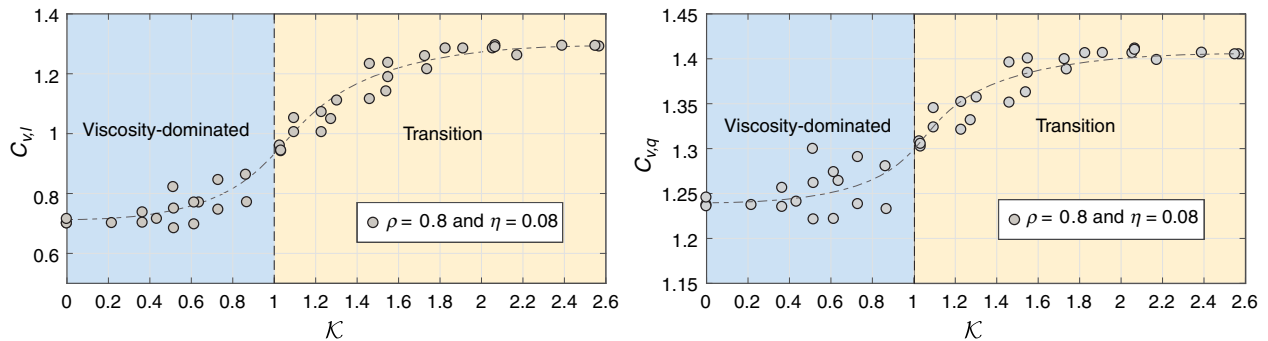


Fig. 6—Simulation results of 42 numerical examples for investigating the influence of dimensionless toughness \mathcal{K} on the coefficients of variation $C_{v,l}$ and $C_{v,q}$. In these examples, $\rho = 0.8$ and $\eta = 0.08$ are fixed, but \mathcal{K} is varied.

The curves of coefficients of variation $C_{v,l}$ and $C_{v,q}$ tend to be steady when the $\mathcal{K} > 2$. Especially, the coefficients of variation for influx $C_{v,q}$ will nearly reach the maximum value $\sqrt{2}$, which indicates that almost all fluid flows into one fracture. In this situation, the shorter fracture will be arrested in a very short time after fracture initiation. A preferential-growth state starts to dominate in the transition regime $\mathcal{K} > 2$, let alone in the toughness-dominated regime ($\mathcal{K} > 4$). In other words, the increasing rock toughness may eliminate the possibility of simultaneous fracture growth.

The scaled fracture footprints S for two examples with $\mathcal{K} = 0.4346$ and $\mathcal{K} = 2.1731$ are provided in Fig. 7. In both examples, the dimensionless parameters are the same except the dimensionless toughness $\mathcal{K} = 0.4346$ and $\mathcal{K} = 2.1731$. The initial fracture settings are the same as Fig. 6 ($\rho = 0.8$, $\eta = 0.08$). In the case of $\mathcal{K} = 0.4346$, the shorter fracture keeps growing slowly to reach a scaled half-length $L_1 = 0.642$, while $L_2 = 1.956$, in which L_i is defined as the half-length scaled by fracture spacing. By contrast, in the case of $\mathcal{K} = 2.1731$, the shorter fracture basically stops its growth immediately after fracture initiation, leading to a small-scaled half-length $L_1 = 0.115$.

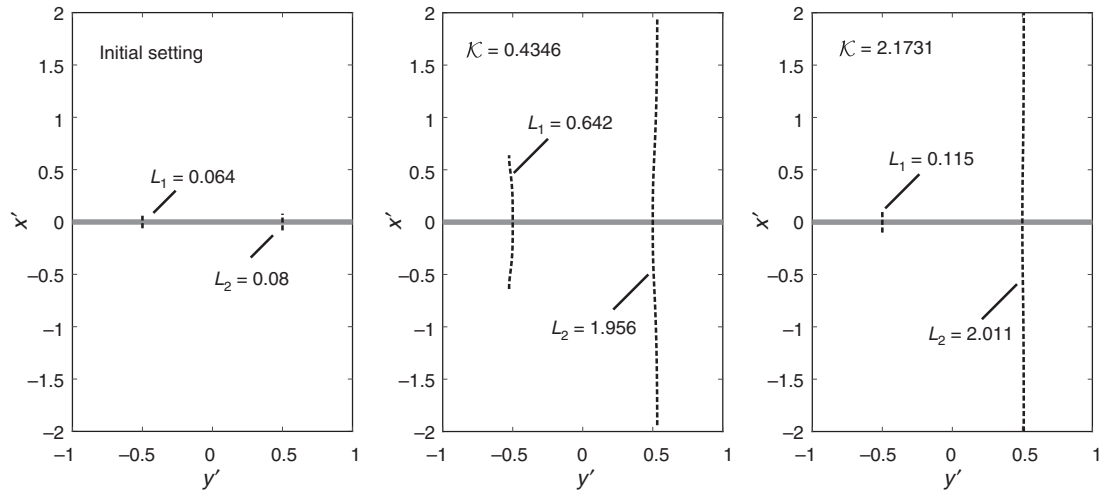


Fig. 7—Scaled fracture footprints S of two examples with $\mathcal{K} = 0.4346$ and $\mathcal{K} = 2.1731$. The initial fracture setting is $\eta = 0.08$, $\rho = 0.8$. An early-time simultaneous-growth pattern is shown in case $\mathcal{K} = 0.4346$. A complete single-fracture-growth pattern is shown in case $\mathcal{K} = 2.1731$.

It is worth noting that, even in the case of no rock toughness ($\mathcal{K} = 0$), the coefficients of variation $C_{v,l}$ and $C_{v,q}$ are still much larger than zero as shown in Fig. 6, representing a remarkable difference in length and influx between two fractures. A higher fluid viscosity can promote the short-fracture growth only in early time, but it cannot help it to catch up with the longer fracture. At a later stage, the growth speed of the shorter fracture in our computations demonstrates a decreasing trend.

Initial Fracture Geometric Setting. In addition to dimensionless toughness \mathcal{K} , initial fracture geometric settings can affect growth competition by varying the dimensionless parameters ρ and η . In this subsection, we study further how ρ and η influence the growth competition.

Initial Half-Length Ratio ρ . Fifty numerical examples are considered to study the effect of initial half-length ratio ρ . In these numerical examples, fracturing spacing D and initial fracture half-length are varied accordingly to keep a fixed $\eta = 0.08$ but different $\rho = 0.4, 0.6, 0.8$, and 0.9 . Fig. 8 shows all the simulation results by plotting the variations of $C_{v,l}$ and $C_{v,q}$ with ρ and \mathcal{K} . It must be highlighted that 42 examples in The Influence of Dimensionless Toughness \mathcal{K} subsection are also included in Fig. 8, indicated by gray dots.

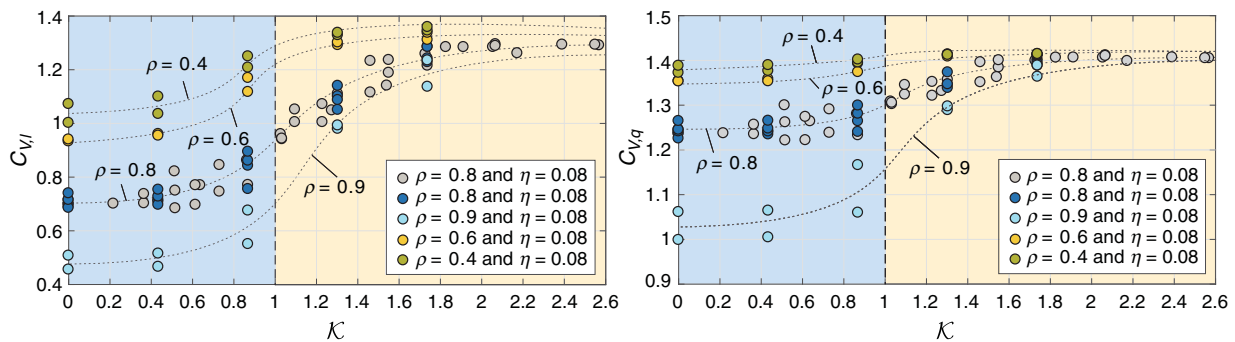


Fig. 8—Simulation results of numerical examples for investigating the influence of initial half-length ratio ρ on the coefficients of variation $C_{v,l}$ and $C_{v,q}$. In numerical examples, $\eta = 0.08$ is fixed, and ρ is varied as 0.4, 0.6, 0.8, and 0.9. For comparison, 42 previous examples of The Influence of Dimensionless Toughness \mathcal{K} subsection are also represented by gray dots.

One can observe that the simulation results of $\rho = 0.8$ and $\eta = 0.08$ are well-gathered around the same S-type curve, as discussed in The Influence of Dimensionless Toughness \mathcal{K} subsection. Although distinct fracture spacings and initial half-lengths are adopted for the newly added results, the collective responses in light of the S-type curves of $C_{v,l}$ and $C_{v,q}$ are the same. It means that the dimensionless

parameter ρ controls the competition in fracture growth. In addition, Fig. 8 shows that, similar to $\rho = 0.8$, S-type curves exist for $\rho = 0.4, 0.6$, and 0.9 and demonstrate that the coefficients of variation $C_{v,l}$ and $C_{v,q}$ increase with decreasing ρ . Not surprisingly, a larger difference in initial fracture lengths will act against the generation of simultaneous growth. Thus, an initial half-length ratio ρ closer to 1.0 is favorable to produce a simultaneous growth, especially in a viscosity-dominated regime.

Actually, when $\rho = 1.0$, two fractures can repel each other, and they can propagate in the same length so that $C_{v,l} \equiv 0$ and $C_{v,q} \equiv 0$ (Zhang et al. 2014). However, this situation cannot be satisfied in the field. When ρ is slightly less than 1.0, the propagation responses demonstrate a strong dependence on \mathcal{K} . On the other hand, when ρ is as small as 0.4, $C_{v,q}$ tends to be $\sqrt{2}$, as shown in Fig. 8, which means that the influx to the shorter fracture approaches zero, even in a viscosity-dominated regime. To generate two nearly equal fractures, the value of ρ should be close to 1.0, and the value of \mathcal{K} should be minimized.

In Fig. 9, we plot the scaled fracture footprints S for two examples with $\rho = 0.4$ and $\rho = 0.9$ when $\mathcal{K} = 0.4346$ and $\eta = 0.08$. In the case of $\rho = 0.4$, the shorter fracture only grows for a very short time to a small-scaled half-length $L_1 = 0.308$. By contrast, in the case of $\rho = 0.9$, the shorter fracture can propagate to a scaled half-length $L_1 = 0.945$. This comparison confirms that a small difference in initial half-lengths can result in a large difference in the eventual fracture lengths.

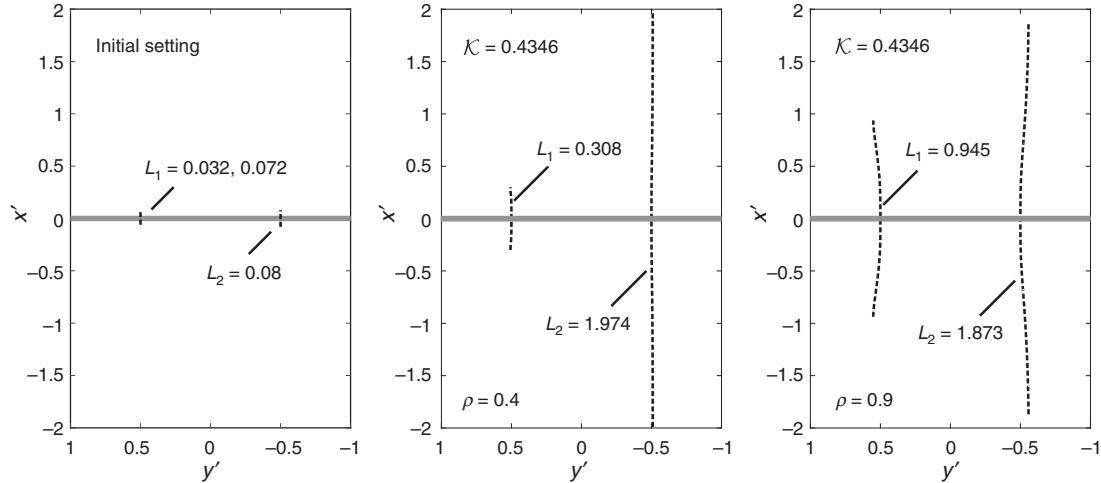


Fig. 9—Scaled fracture footprints S of two examples with $\rho = 0.4$ and $\rho = 0.9$. In both examples, the fracture propagation is in a viscosity-dominated regime ($\mathcal{K} = 0.4346$). A preferential-growth pattern is shown in case $\rho = 0.4$. By contrast, a relatively simultaneous growth pattern is shown in case $\rho = 0.9$.

Initial Half-Length Spacing Ratio η . To investigate the influence of the initial half-length-spacing ratio η , 25 more numerical examples are performed. In these examples, different values of $\eta = 0.04, 0.1$, and 0.16 are considered by varying the fracturing spacing and initial fracture half-length. We plot the variations of $C_{v,l}$ and $C_{v,q}$ in Fig. 10. For comparison, previous numerical examples with $\eta = 0.08$ are also shown in this figure. It can be observed that a reduction in η can increase the values of $C_{v,l}$ and $C_{v,q}$, but it does not have a strong influence on the coefficients of variation $C_{v,l}$ and $C_{v,q}$. One should note that there is an underlying assumption behind this conclusion that the half-length spacing ratio η should be significantly less than 1.0, which is reasonable for most fracturing treatments.

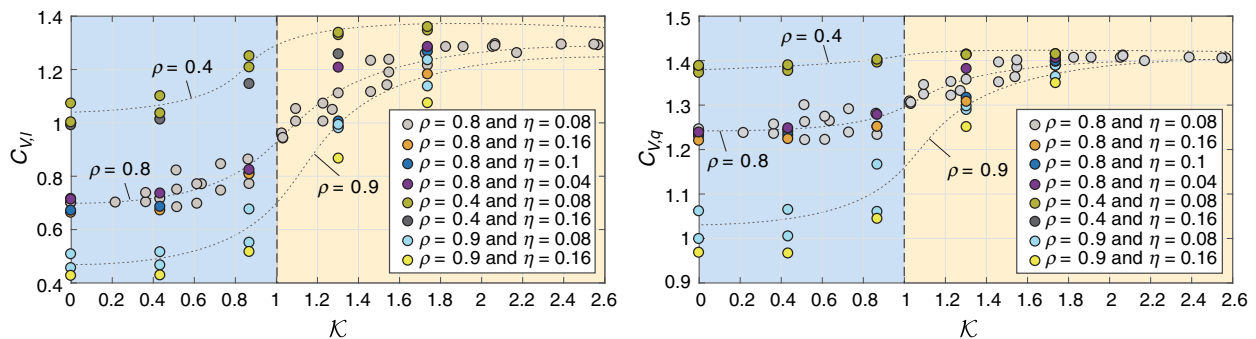


Fig. 10—Simulation results of numerical examples for investigating the influence of initial half-length spacing ratio η on the coefficients of variation $C_{v,l}$ and $C_{v,q}$. In these examples, $\eta = 0.04, 0.1$, and 0.16 are adopted. For comparison, previous numerical examples with $\eta = 0.08$ are also shown in this figure.

Fracture Deflection. Although the previous discussion has not included the dimensionless differential stress χ , which compares the magnitude of the far-field differential stress to the induced stress, χ can affect the fracture footprints S in the growth competition between two fractures. In this subsection, we investigate the effect of the dimensionless differential stress χ on the fracture-propagation path. Specifically, we will use the dimensionless differential stresses, χ_m and χ_k , respectively, for two limiting cases.

Viscosity-Dominated Regime. First, χ_m , which represents the ratio of the far-field stress to the stress induced by the viscous dissipation, is used for investigating the viscosity-dominated regime case. In Fig. 11a, the scaled fracture footprints S of five numerical examples with fixed $\chi_m = 0.609$ are plotted. Four of these examples have the same initial half-length ratio $\rho = 0.9$ but different dimensionless toughness $\mathcal{K} = 0, 0.4346, 0.8092, 1.3039$. The other example has $\rho = 0.4$ and $\mathcal{K} = 0.4346$.

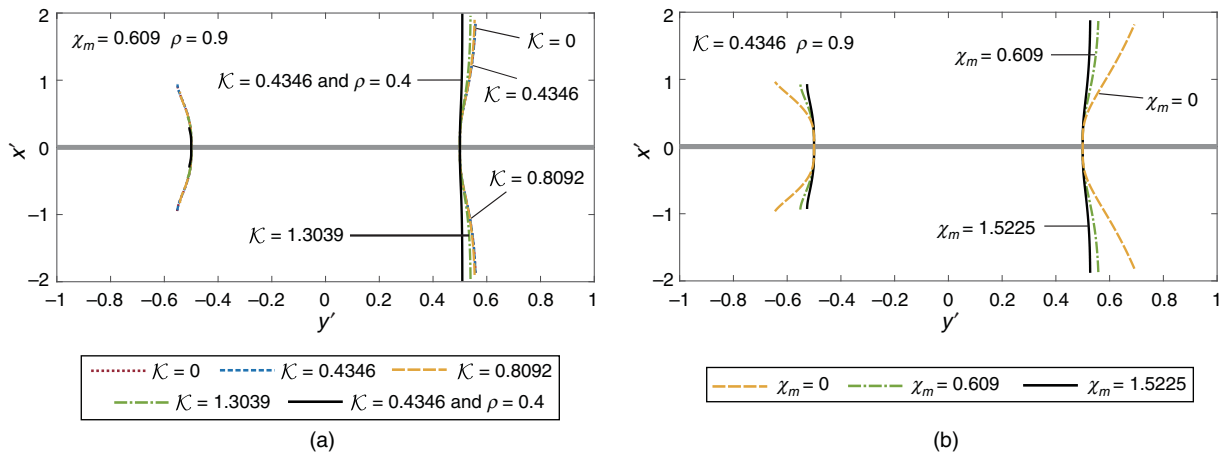


Fig. 11—Simulation results of numerical examples for investigating the influence of dimensionless differential stress χ_m on the fracture-propagation path. (a) The scaled fracture footprints of five numerical examples, respectively, corresponding to $\kappa = 0, 0.4346, 0.8092, 1.3039$ at $\rho = 0.9$ and $\kappa = 0.4346$ at $\rho = 0.4$. The dimensionless differential stress χ_m is fixed as 0.609. (b) The scaled fracture footprints of three numerical examples, respectively, corresponding to $\chi_m = 0, 0.609, 1.5225$; $\kappa = 0.4346$; and $\rho = 0.9$.

It is interesting to observe that three examples with $\kappa < 1$ and $\rho = 0.9$ produce almost the same curved fracture footprint at $\chi_m = 0.609$. However, in another example with $\kappa = 1.3039$ and $\rho = 0.9$ (green line, Fig. 11), the growth of the shorter fracture is constrained, and the fracture footprint of the longer one curves more gradually, which is attributed to the larger $\kappa > 1$. The fracture-propagation-path difference can be governed by the dimensionless parameter χ_m in the viscosity-dominated regime $\kappa < 1$. Similarly, the example with $\kappa = 0.4346$ and $\rho = 0.4$ (black line) shows a small shorter fracture and a nearly straight path of longer fractures. As indicated by the previous discussions, a small value of ρ also will limit the short fracture growth and thus change the deflection extent, as does a large value of κ .

We plot the scaled fracture footprints of three examples with the same $\kappa = 0.4346$ and $\rho = 0.9$ but at different $\chi_m = 0, 0.609, 1.5225$ in Fig. 11b. As shown in Fig. 11b, the fracture-deflection extent is gradually reduced with increasing χ_m , and thus nearly parallel fracture paths with similar growth extents can be generated by a high χ_m . Note that to keep $\kappa < 1$ for simultaneous fracture growth, higher fluid viscosity and higher injection rates are needed, and thus the possible way to effectively increase χ_m is the choice of the fracturing site with a higher far-field differential stress $\Delta\sigma$.

Toughness-Dominated Regime and Transition Regime. The parameter χ_m cannot be used to quantitatively characterize the fracture path when $\kappa > 1$ (Bunger et al. 2012), as shown in previous simulations. It is therefore natural to further use χ_k to replace χ_m in the following discussion. When κ is larger than 2.0, the condition $\rho = 1.0$ is the only way to propagate the shorter fracture to a noticeable distance, as discussed previously; thus, we set $\rho = 1.0$ in the following examples. The scaled fracture footprints S of four numerical examples with fixed $\chi_k = 0.2802$, $\rho = 1.0$, and different $\kappa = 1.4533, 3.3261, 4.1824, 5.2591$ are shown in Fig. 12a. It can be observed that the fracture footprints are almost independent of the value of κ , and then χ_k becomes the sole parameter in characterizing the final fracture footprints.

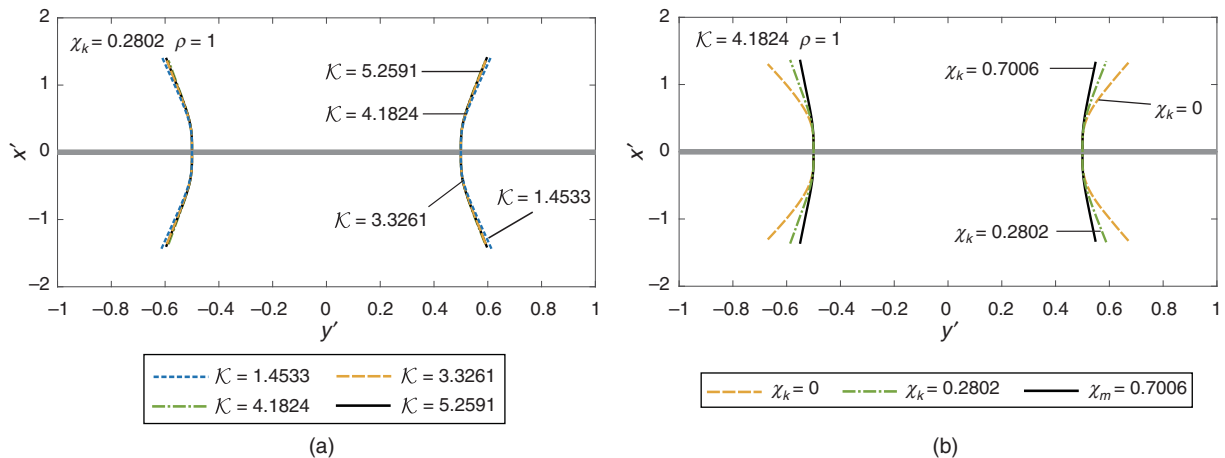


Fig. 12—Simulation results of numerical examples for investigating the influence of dimensionless differential stress χ_k on the fracture-propagation path. (a) The scaled fracture footprints of four numerical examples, respectively, corresponding to $\kappa = 1.4533, 3.3261, 4.1824, 5.2591$; $\chi_k = 0.2802$; and $\rho = 1$. (b) The scaled fracture footprints of three numerical examples corresponding to $\chi_k = 0, 0.2802, 0.7006$; $\kappa = 4.1824$; and $\rho = 1$.

In Fig. 12b, we plot the scaled fracture footprints of three examples with the same values of $\kappa = 4.1824$ and different values of $\chi_k = 0, 0.2802, 0.7006$. A significant reduction of fracture-deflection extents can be found with increasing χ_k . Therefore, at larger κ and $\rho = 1.0$, nearly parallel fracture paths can also be produced by higher dimensionless differential stress χ_k .

Field Implications

In the past decade, engineers always attempted to find a way to generate the simultaneous growth of closely spaced fractures in the petroleum industry (e.g., using additive tools to equally divide the injection-fluid rates into each fracture). Here, we only explore the favorable conditions for simultaneous fracture growth in terms of geomechanics modeling results, without considering any other mechanical factors. Even in the early-time fracture growth, to promote fracture-growth extent as far as possible is very important because the shorter fracture can provide an additional conductive channel for fluid to reach the natural fractures in reservoir rocks, which is important in enhancing reservoir permeability. On the basis of previous parametric analyses, some implications of the numerical results related to promoting simultaneous growth in the field are presented:

- The tendency of preferential growth will increase with increasing dimensionless toughness \mathcal{K} , which is directly proportional to the rock toughness. In early time, the simultaneous growth of closely spaced fractures with less initial length offset can occur only in the case of a viscosity-dominated regime $\mathcal{K} \ll 1$. This implies that a higher viscosity together with a higher injection rate can assist in the simultaneous growth at early time. Although the simultaneous growth will eventually give way to the preferential growth, the continuous growth of a shorter fracture as much as possible also can offer an alternative means to improve rock permeability.
- The initial fracture geometry settings can influence the growth-competition results. In particular, the ratio of the initial fracture half-lengths ρ significantly affects the coefficients of variation $C_{v,l}$ and $C_{v,q}$. A small length offset at the beginning will result in a huge difference in final sizes between two fractures due to the stress-shadow effect. Thus, similar initial fracture sizes are beneficial to promoting the simultaneous growth. In industry, a technology called the plug-and-perforate method is commonly used to generate initial fractures. However, with this technology, initial fractures caused by the shots of the perforation gun typically have irregular sizes. For promoting simultaneous growth, a possible alternative method is to notch the wellbore, using specialized equipment, for generating more regular initial fractures. Furthermore, another advantage of the notched wellbore is that it may reduce the fracture tortuosity near the wellbore, which can also lead to a serious preferential growth.
- In fracturing treatment, the curving of the fracture path might lead to the repelling or the coalescence of closely spaced fractures, which will reduce the effectiveness of the fracturing treatment. Thus, man-made hydraulic fractures are always expected to be planar or nearly planar. Parametric analysis shows that the fracture deflection is minimized by a larger far-field differential stress. However, this does not mean that the fracture conductivity can be much increased under a higher differential-stress environment. This is because the natural fracture can play a key role in conducting fluids, and the large differential stress could impede fluid penetration in natural fractures.

As previous parametric analysis shows, a large simultaneous-growth extent is difficult to attain. In industry, to promote the simultaneous growth, some assistance technologies are often considered. The limited-entry method, which uses a high inlet pressure loss to balance the uneven influx partition, is the most common method used in industry (Lecampion and Desroches 2015a). A diverting agent can work to assist in the growth of a stunted fracture by preventing the fluid flow from entering the preferentially growing fracture. In addition, field investigation and numerical simulations show that optimized perforation placement is also beneficial to the simultaneous growth (Peirce and Bunger 2015). However, the effectiveness of these methods, used for countering the preferential growth, has not shown a good robustness in practice to date. Their success is quite sensitive to the geological-parameter characterization and engineering design. A novel method with the ability to keep a sustained simultaneous-growth pattern is needed urgently.

In essence, the reason for the difficulty in creating robust simultaneous fracture growth is that the single hydraulic-fracture growth, in most cases, appears energetically favorable compared with the simultaneous growth, especially at large time in our numerical results. Thus, to resolve this issue, a natural idea is to generate an energetically favorable simultaneous-growth pattern. The energy analysis by Bunger (2013) reveals that the energy-dissipation process, which controls the energy-minimizing growth pattern, is distinct in different fracture-geometry cases (e.g., 2D plane strain, radial, Perkins-Kern-Nordgren). A most-overlooked possibility would be that the fluid-driven fracture geometry can be deliberately designed to reach an energetically favorable simultaneous-growth pattern. This interesting issue, which is beyond the scope of this paper, will be our focus in future work.

Conclusions

In this paper, we have presented a 2D model to simulate the simultaneous growth of two fluid-driven fractures under the conditions of plane strain. In this model, we adopted both the displacement discontinuity method and the finite volume method to solve this fluid/solid coupling problem. A key feature of this 2D model is the use of a universal tip asymptotic solution, which represents the unique multi-scale tip behavior of fluid-driven fractures, as a propagation criterion to properly locate the fracture front. This treatment makes the model deal with fluid-driven fracture problems in arbitrary parameter groups. As expected, our numerical results match well with analytical solutions in the viscosity-dominated regime, the transition regime, and the toughness-dominated regime.

The modeling results are provided that two fractures propagate symmetrically regarding the well. The early-time fracture growth is considered, and the simultaneous fracture growth is characterized by the coefficients of variation related to the lengths and the influxes of two fractures. The propagation of the shorter fracture to a certain distance can facilitate the permeability enhancement of rocks because it can provide an additional channel connecting the well and the natural-fracture networks. Thus, it is worthwhile to investigate the feasibility of the shorter fracture growth although it eventually will be dominated by the longer fracture growth.

The scaling analysis is given and demonstrates that the competition between two fractures to grow depends on four dimensionless parameters ($\mathcal{K}, \chi, \rho, \eta$), the first two of which are related to the material and loading parameters and the last two are associated with initial fracture-geometry settings. The numerical results for more than 100 examples support the use of higher fluid viscosity, higher injection rates, and nearly equal initial fracture length to obtain relatively uniform simultaneous fracture growth. Compared with the fracture-length ratio ρ , the ratio of the initial fracture half-length to fracture spacing η seems less important, possibly because the initial fracture size is always much smaller than the fracture spacing in real treatments. In addition, a large far-field differential stress has the ability to reduce the curving extent of closely spaced fractures; however, the use of this feature is debatable because it might prevent the formation of complex fracture networks.

One must note that the previous conclusions are valid on the basis of the assumptions used. For inapplicable cases, care should be taken in applying the previous conclusions.

Nomenclature

$c_{nn}, c_{ns}, c_{sn}, c_{ss}$ = hypersingular Green's functions

$C_{v,l}, C_{v,q}$ = coefficients of variation for half-lengths and influxes of two fractures

D = fracture spacing, m
 E, E' = Young's modulus, MPa
 j = serial number of mesh
 k = permeability, md
 K_{IC}, K_I' = rock toughness, MPa·m^{0.5}
 K_I, K_{II} = Mode I and II stress-intensity factors, MPa·m^{0.5}
 l_1, l_2 = initial fracture lengths for two fractures, m
 l_e = mesh length, m
 l_{mk} = characteristic length, m
 \bar{l} = mean value for half-lengths of two fractures, m
 L_1, L_2 = scaled fracture half-lengths
 p = fluid pressure in fracture, MPa
 p_i = inlet fluid pressure for i th fracture, MPa
 p^{inlet} = fracture-inlet pressure, MPa
 p^{wf} = pressure drop caused by wellbore friction, MPa
 p^{pf} = pressure drop caused by perforation friction, MPa
 q = fluid-flow rate in fracture, m³/s
 q_i = inlet flux rate for i th fracture, m³/s
 Q = fluid-injection rate, m³/s
 r, r_o = distances to the fracture tip at current timestep and last timestep, m
 S = fracture footprint
 $t, \Delta t$ = time and timestep, seconds
 v = fracture-surface shear displacement, m
 V = propagation velocity, m/s
 \bar{V}_q = mean value for influxes of two fractures, m³
 w, w_o = fracture openings at current timestep and last timestep, m
 x, y = Cartesian coordinates, m
 x', y' = scaled Cartesian coordinates
 δ = Dirac delta function
 ε = dimensionless small number
 η = ratio of longer initial fracture half-length to fracture spacing
 θ = local fracture-deflection angle
 κ = ratio of Mode II stress-intensity factor to Mode I stress-intensity factor
 \mathcal{K} = dimensionless toughness
 μ, μ' = fluid viscosity, MPa·s
 ν = Poisson's ratio
 ξ = length scale, m
 σ_c^n = normal-direction components of horizontal far-field stress, MPa
 σ_c^s = shear-direction components of horizontal far-field stress, MPa
 $\sigma_{c,min}$ = minimum horizontal far-field stress, MPa
 $\Delta\sigma$ = far-field differential stress, MPa
 ς_l = standard deviation for half-lengths of two fractures, m
 ς_v = standard deviation for influxes of two fractures, m³
 ρ = ratio of two initial fracture half-lengths
 χ_m, χ_k = dimensionless differential stress

Acknowledgments

The authors gratefully acknowledge the support of the Major Program of the National Natural Science Foundation of China (Grant No. 51490653) and Sichuan Youth Science and Technology Innovation Research Team Program (2017TD0013). Xiyu Chen gratefully acknowledges the support of Southwest Petroleum University for sponsoring the visit to Monash University and the CSIRO to complete this research study.

References

- Adachi, J. I. 2001. *Fluid-Driven Fracture in Permeable Rock*. Dissertation, University of Minnesota, Minneapolis. <https://elibrary.ru/item.asp?id=5261032>.
- Adachi, J. I. and Detournay, E. 2008. Plane Strain Propagation of a Hydraulic Fracture in a Permeable Rock. *Engineering Fracture Mechanics* **75** (16): 4666–4694. <https://doi.org/10.1016/j.engfracmech.2008.04.006>.
- Bell, F. G. 2004. *Engineering Geology and Construction*. CRC Press.
- Bunger, A. P. and Cruden, A. R. 2011. Modeling the Growth of Laccoliths and Large Mafic Sills: Role of Magma Body Forces. *Journal of Geophysical Research: Solid Earth* **116** (B2). <https://doi.org/10.1029/2010JB007648>.
- Bunger, A. P., Zhang, X., and Jeffrey, R. G. 2012. Parameters Affecting the Interaction Among Closely Spaced Hydraulic Fractures. *SPE J.* **17** (1): 292–306. SPE-140426-PA. <https://doi.org/10.2118/140426-PA>.
- Bunger, A. P. 2013. Analysis of the Power Input Needed to Propagate Multiple Hydraulic Fractures. *International Journal of Solids and Structures* **50** (10): 1538–1549. <https://doi.org/10.1016/j.ijsolstr.2013.01.004>.
- Bunger, A., Jeffrey, R. G., and Zhang, X. 2014. Constraints on Simultaneous Growth of Hydraulic Fractures From Multiple Perforation Clusters in Horizontal Wells. *SPE J.* **19** (4): 608–620. SPE-163860-PA. <https://doi.org/10.2118/163860-PA>.
- Bunger, A. P. and Peirce, A. P. 2014. Numerical Simulation of Simultaneous Growth of Multiple Interacting Hydraulic Fractures From Horizontal Wells. In *Shale Energy Engineering 2014: Technical Challenges, Environmental Issues, and Public Policy*. pp. 201–210. <https://doi.org/10.1061/9780784413654.021>.
- Bunger, A. and Lecampion, B. 2017. *Four Critical Issues for Successful Hydraulic Fracturing Applications*. Tech. rep., CRC Press.

- Crouch, S. L. and Starfield, A. M. 1983. *Boundary Element Methods in Solid Mechanics: With Applications in Rock Mechanics and Geological Engineering*. Vol. 50. Winchester, Massachusetts: George Allen and Unwin.
- Crump, J. B. and Conway, M. W. 1988. Effects of Perforation-Entry Friction on Bottomhole Treating Analysis. *J Pet Technol* **40** (8): 1041–1048. SPE-15474-PA. <https://doi.org/10.2118/15474-PA>.
- Daneshy, A. A. 2015. Dynamic Interaction Within Multiple Limited Entry Fractures in Horizontal Wells: Theory, Implications, and Field Verification. Presented at the SPE Hydraulic Fracturing Technology Conference, The Woodlands, Texas, USA, 3–5 February. SPE-173344-MS. <https://doi.org/10.2118/173344-MS>.
- Detournay, E. 2004. Propagation Regimes of Fluid-Driven Fractures in Impermeable Rocks. *International Journal of Geomechanics* **4** (1): 35–45. [https://doi.org/10.1061/\(ASCE\)1532-3641\(2004\)4:1\(35\)](https://doi.org/10.1061/(ASCE)1532-3641(2004)4:1(35)).
- Detournay, E. 2016. Mechanics of Hydraulic Fractures. *Annual Review of Fluid Mechanics* **48**: 311–339. <https://doi.org/10.1146/annurev-fluid-010814-014736>.
- Dontsov, E. V. and Peirce, A. P. 2015. A Non-Singular Integral Equation Formulation to Analyze Multiscale Behaviour in Semi-Infinite Hydraulic Fractures. *Journal of Fluid Mechanics* **781** (R1). <https://doi.org/10.1017/jfm.2015.451>.
- East, L., Soliman, M. Y., Augustine, J. R. et al. 2011. Methods for Enhancing Far-Field Complexity in Fracturing Operations. *SPE Prod & Oper* **26** (3): 291–303. SPE-133380-PA. <https://doi.org/10.2118/133380-PA>.
- Economides, M. J., Nolte, K. G., Ahmed, U. et al. 2000. *Reservoir Stimulation*. Vol. 18. Wiley Chichester.
- Elbel, J., Piggott, A., Mack, M. et al. 1992. Numerical Modeling of Multilayer Fracture Treatments. Presented at the Permian Basin Oil and Gas Recovery Conference, Midland, Texas, USA, 18–20 March. SPE-23982-MS. <https://doi.org/10.2118/23982-MS>.
- Erdogan, F. and Sih, G. C. 1963. On the Crack Extension in Plates Under Plane Loading and Transverse Shear. *Journal of Basic Engineering* **85** (4): 519–525. <https://doi.org/10.1115/1.3656897>.
- Fisher, M. K., Heinze, J. R., Harris, C. D. et al. 2004. Optimizing Horizontal Completion Techniques in the Barnett Shale Using Microseismic Fracture Mapping. Presented at the SPE Annual Technical Conference and Exhibition, Houston, 26–29 September. SPE-90051-MS. <https://doi.org/10.2118/90051-MS>.
- Garagash, D. I., Detournay, E., and Adachi, J. I. 2011. Multiscale Tip Asymptotics in Hydraulic Fracture With Leak-Off. *Journal of Fluid Mechanics* **669**: 260–297. <https://doi.org/10.1017/S002211201000501X>.
- Germanovich, L. N. and Astakhov, D. K. 2004. Fracture Closure in Extension and Mechanical Interaction of Parallel Joints. *Journal of Geophysical Research: Solid Earth* (1978–2012) **109** (B2). <https://doi.org/10.1029/2002JB002131>.
- Howard, G. C. and Fast, C. 1957. Optimum Fluid Characteristics for Fracture Extension. In *Drilling and Production Practice*. API-57-261. New York: American Petroleum Institute.
- Jeffrey, R. G., Chen, Z., Mills, K. W. et al. 2013. Monitoring and Measuring Hydraulic Fracturing Growth During Preconditioning of a Roof Rock Over a Coal Longwall Panel. In *Effective and Sustainable Hydraulic Fracturing*. Chapter 45. InTech. <https://doi.org/10.5772/56325>.
- King, G. 2010. Thirty Years of Gas Shale Fracturing: What Have We Learned? Presented at the SPE Annual Technical Conference and Exhibition, Florence, Italy, 19–22 September. SPE-133456-MS. <https://doi.org/10.2118/133456-MS>.
- Lecampion, B. and Desroches, J. 2015a. Robustness to Formation Geological Heterogeneities of the Limited-Entry Technique for Multi-Stage Fracturing of Horizontal Wells. *Rock Mechanics and Rock Engineering* **48** (6): 2637–2644. <https://doi.org/10.1007/s00603-015-0836-5>.
- Lecampion, B. and Desroches, J. 2015b. Simultaneous Initiation and Growth of Multiple Radial Hydraulic Fractures From a Horizontal Wellbore. *Journal of the Mechanics and Physics of Solids* **82**: 235–258. <https://doi.org/10.1016/j.jmps.2015.05.010>.
- Legarth, B., Huenges, E., and Zimmermann, G. 2005. Hydraulic Fracturing in a Sedimentary Geothermal Reservoir: Results and Implications. *International Journal of Rock Mechanics and Mining Sciences* **42** (7): 1028–1041. <https://doi.org/10.1016/j.ijrmms.2005.05.014>.
- Meyer, B. R. and Bazan, L. W. 2011. A Discrete Fracture Network Model for Hydraulically Induced Fractures—Theory, Parametric and Case Studies. Presented at the SPE Hydraulic Fracturing Technology Conference, The Woodlands, Texas, USA, 24–26 January. SPE-140514-MS. <https://doi.org/10.2118/140514-MS>.
- Miller, C. K., Waters, G. A., Rylander, E. I. et al. 2011. Evaluation of Production Log Data From Horizontal Wells Drilled in Organic Shales. Presented at the North American Unconventional Gas Conference and Exhibition, The Woodlands, Texas, USA, 14–16 June. SPE-144326-MS. <https://doi.org/10.2118/144326-MS>.
- Nagel, N. B. and Sanchez-Nagel, M. 2011. Stress Shadowing and Microseismic Events: A Numerical Evaluation. Presented at the SPE Annual Technical Conference and Exhibition, Denver, 30 October–2 November. SPE-147363-MS. <https://doi.org/10.2118/147363-MS>.
- Olson, J. E. 2008. Multi-Fracture Propagation Modeling: Applications to Hydraulic Fracturing in Shales and Tight Gas Sands. Presented at the 42nd US Rock Mechanics Symposium (USRMS), San Francisco, 29 June–2 July. ARMA-08-327.
- Peirce, A. and Detournay, E. 2008. An Implicit Level Set Method for Modeling Hydraulically Driven Fractures. *Computer Methods in Applied Mechanics and Engineering* **197** (33): 2858–2885. <https://doi.org/10.1016/j.cma.2008.01.013>.
- Peirce, A. and Bunger, A. 2015. Interference Fracturing: Non-Uniform Distributions of Perforation Clusters That Promote Simultaneous Growth of Multiple Hydraulic Fractures. *SPE J.* **20** (2): 384–395. SPE-172500-PA. <https://doi.org/10.2118/172500-PA>.
- Pollard, D. D. and Holzhausen, G. 1979. On the Mechanical Interaction Between a Fluid-Filled Fracture and the Earth's Surface. *Tectonophysics* **53** (1–2): 27–57. [https://doi.org/10.1016/0040-1951\(79\)90353-6](https://doi.org/10.1016/0040-1951(79)90353-6).
- Rice, J. R. 1985. First-Order Variation in Elastic Fields Due to Variation in Location of a Planar Crack Front. *Journal of Applied Mechanics* **52** (3): 571–579. <https://doi.org/10.1115/1.3169103>.
- Roper, S. M. and Lister, J. R. 2005. Buoyancy-Driven Crack Propagation From an Over-Pressured Source. *Journal of Fluid Mechanics* **536**: 79–98. <https://doi.org/10.1017/S0022112005004337>.
- Roussel, N. P. and Sharma, M. M. 2011. Strategies to Minimize Frac Spacing and Stimulate Natural Fractures in Horizontal Completions. Presented at the SPE Annual Technical Conference and Exhibition, Denver, 30 October–2 November. SPE-146104-MS. <https://doi.org/10.2118/146104-MS>.
- Rubin, A. M. 1995. Propagation of Magma-Filled Cracks. *Annual Review of Earth and Planetary Sciences* **23** (1): 287–336. <https://doi.org/10.1146/annurev.ea.23.050195.001443>.
- Sesetty, V. and Ghassemi, A. 2016. Numerical Modeling of Hydraulic Fracture Propagation From Horizontal Wells in Anisotropic Shale. Presented at the 50th US Rock Mechanics/Geomechanics Symposium, Houston, 26–29 June. American Rock Mechanics Association, ARMA-2016-181.
- Siriwardane, H. and Layne, A. 1991. Improved Model for Predicting Multiple Hydraulic Fracture Propagation From a Horizontal Well. Presented at the SPE Eastern Regional Meeting, Lexington, Kentucky, USA, 22–25 October. SPE-23448-MS. <https://doi.org/10.2118/23448-MS>.
- Somanchi, K., O'Brien, C., Huckabee, P. et al. 2016. Insights and Observations Into Limited Entry Perforation Dynamics From Fiber-Optic Diagnostics. Presented at the SPE/AAPG/SEG Unconventional Resources Technology Conference, San Antonio, Texas, USA, 1–3 August. URTEC-2458389-MS. <https://doi.org/10.15530/URTEC-2016-2458389>.
- Spence, D. A. and Sharp, P. 1985. Self-Similar Solutions for Elastohydrodynamic Cavity Flow. In *Proc., the Royal Society of London A: Mathematical, Physical, and Engineering Sciences*. Vol. 400. The Royal Society, pp. 289–313, 1819.

- Spence, D. A., Sharp, P. W., and Turcotte, D. L. 1987. Buoyancy-Driven Crack Propagation: A Mechanism for Magma Migration. *Journal of Fluid Mechanics* **174**: 135–153. <https://doi.org/10.1017/S0022112087000077>.
- Tsai, V. C. and Rice, J. R. 2010. A Model for Turbulent Hydraulic Fracture and Application to Crack Propagation at Glacier Beds. *Journal of Geophysical Research: Earth Surface* **115** (F3). <https://doi.org/10.1029/2009JF001474>.
- Ugueto, C., Gustavo, A., Huckabee, P. T. et al. 2016. Perforation Cluster Efficiency of Cemented Plug and Perf Limited Entry Completions; Insights From Fiber Optics Diagnostics. Presented at the SPE Hydraulic Fracturing Technology Conference, The Woodlands, Texas, USA, 9–11 February. SPE-179124-MS. <https://doi.org/10.2118/179124-MS>.
- Valk, P. and Economides, M. J. 1995. *Hydraulic Fracture Mechanics*. New York: Wiley.
- Wu, K. and Olson, J. E. 2015. Simultaneous Multifracture Treatments: Fully Coupled Fluid Flow and Fracture Mechanics for Horizontal Wells. *SPE J.* **20** (2): 337–346. SPE-167626-PA. <https://doi.org/10.2118/167626-PA>.
- Wu, K., Olson, J., Balhoff, M. T. et al. 2017. *Numerical Analysis for Promoting Uniform Development of Simultaneous Multiple-Fracture Propagation in Horizontal Wells*. Vol. 32. pp. 41–50. Richardson, Texas: Society of Petroleum Engineers.
- Zeng, Q., Liu, Z., Wang, T. et al. 2018. Fully Coupled Simulation of Multiple Hydraulic Fractures to Propagate Simultaneously From a Perforated Horizontal Wellbore. *Computational Mechanics* **61** (1–2): 137–155. <https://doi.org/10.1007/s00466-017-1412-5>.
- Zhang, X. and Jeffrey, R. G. 2012. Fluid-Driven Multiple Fracture Growth From a Permeable Bedding Plane Intersected by an Ascending Hydraulic Fracture. *Journal of Geophysical Research: Solid Earth* **117** (B12). <https://doi.org/10.1029/2012JB009609>.
- Zhang, X., Bunger, A. P., and Jeffrey, R. G. 2014. Mechanics of Two Interacting Magma-Driven Fractures: A Numerical Study. *Journal of Geophysical Research: Solid Earth* **119** (11): 8047–8063. <https://doi.org/10.1002/2014JB011273>.
- Zhao, J., Chen, X., Li, Y. et al. 2016. Simulation of Simultaneous Propagation of Multiple Hydraulic Fractures in Horizontal Wells. *Journal of Petroleum Science and Engineering* **147**: 788–800. <https://doi.org/10.1016/j.petrol.2016.09.021>.
- Zhao, J., Chen, X., Li, Y. et al. 2017. Numerical Simulation of Multi-Stage Fracturing and Optimization of Perforation in a Horizontal Well. *Petroleum Exploration and Development* **44** (1): 119–126. [https://doi.org/10.1016/S1876-3804\(17\)30015-0](https://doi.org/10.1016/S1876-3804(17)30015-0).

Appendix A: Elasto-Hydrodynamics-Coupling Solver

For completeness, here we simply discuss the method for solving the elasto-hydrodynamics-coupling problem in the model. By adopting the displacement discontinuity method, the elasticity equation (Eq. 2) can be rewritten as

$$\begin{bmatrix} \mathbf{C}_{nn} & \mathbf{C}_{ns} \\ \mathbf{C}_{sn} & \mathbf{C}_{ss} \end{bmatrix} \begin{bmatrix} \mathbf{w} \\ \mathbf{v} \end{bmatrix} = \begin{bmatrix} \mathbf{p} \\ 0 \end{bmatrix} - \begin{bmatrix} \boldsymbol{\sigma}_c^n \\ \boldsymbol{\sigma}_c^s \end{bmatrix}, \quad \text{..... (A-1)}$$

where \mathbf{w} , \mathbf{v} , \mathbf{p} are vectors of fracture opening, shear displacement, and fluid pressure. The details of coefficient matrix \mathbf{C}_{ss} , \mathbf{C}_{ns} ... are presented in Crouch and Starfield (1983). First, we rewrite Eq. A-1 as a linear system.

$$\mathbf{p} = \mathbf{C}\mathbf{w} + \boldsymbol{\sigma}, \quad \text{..... (A-2)}$$

in which

$$\mathbf{C} = \mathbf{C}_{nn} - \mathbf{C}_{ns}\mathbf{C}_{ss}^{-1}\mathbf{C}_{sn} \quad \boldsymbol{\sigma} = \boldsymbol{\sigma}_c^n - \mathbf{C}_{ns}\mathbf{C}_{ss}^{-1}\boldsymbol{\sigma}_c^s. \quad \text{..... (A-3)}$$

Similarly, on the basis of the finite volume method, the lubrication equation (Eq. 8) and the continuity equation (Eq. 9) can be rewritten as

$$\mathbf{w} = \Delta t[\mathbf{B}(\mathbf{w})\mathbf{p}] + \Delta t\mathbf{Q} + \mathbf{w}_0, \quad \text{..... (A-4)}$$

in which \mathbf{w} , \mathbf{w}_0 are vectors of the fracture opening at a current timestep and last timestep and

$$[\mathbf{B}(\mathbf{w})\mathbf{p}] = \frac{1}{\mu'l_e} \left[w_{j+\frac{1}{2}}^3 \frac{(p_{j+1} - p_j)}{l_e} - w_{j-\frac{1}{2}}^3 \frac{(p_j - p_{j-1})}{l_e} \right] \text{ and } \mathbf{Q} = \frac{Q\delta}{l_e}, \quad \text{..... (A-5)}$$

where l_e is the mesh length and j is the mesh sequence number. Then, we can combine Eqs. A-2 and A-4 to obtain the governing equation representing the elasto-hydrodynamics coupling as

$$\mathbf{w} = \Delta t[\mathbf{B}(\mathbf{w})(\mathbf{C}\mathbf{w} + \boldsymbol{\sigma})] + \Delta t\mathbf{Q} + \mathbf{w}_0. \quad \text{..... (A-6)}$$

For the nonlinear Eq. A-6, an iterative method can be adopted to obtain the unknown parameter, width \mathbf{w} ; then, the shear displacement \mathbf{v} and the fluid pressure \mathbf{p} in the fracture-growth process can be obtained (Peirce and Detournay 2008).

Appendix B: Multiscale Tip Behavior of Hydraulic Fracture

Fracture propagation is a moving-boundary problem: At each time step, we must update the position of the fracture tip in the numerical simulation. To locate the fracture-tip position, a typical level-set method is to use the relation between the fracture opening w and the distance from the fracture tip r (Peirce and Detournay 2008). With known fracture opening w at a specific mesh near the fracture tip, we can calculate the distance r between the mesh center and the fracture tip, and, hence, update the tip position.

However, the fluid-driven fracture propagation is a multiphysics process; hence, the $w - r$ relation is scale-dependent (Garagash et al. 2011; Detournay 2016). In the tip zone of the hydraulic fracture, the behavior of the part close to the fracture tip is controlled mostly by the fracture-surface creation (fracture toughness), and the behavior of the part intermediately far away from the tip is more likely to be affected by the fluid viscosity (See Fig. B-1). As a result, along the path away from the fracture tip, the $w - r$ relation is gradually transferred from $w \sim r^{1/2}$ to $w \sim V^{1/3}r^{2/3}$.

Garagash et al. (2011) have investigated this multiscale tip behavior of a fluid-driven fracture, and they presented a characteristic length l_{mk} for fluid-driven fracture propagation in impermeable rock,

$$l_{mk} = \frac{K_I'^6}{E'^4\mu'^2V^2}. \quad \text{..... (B-1)}$$

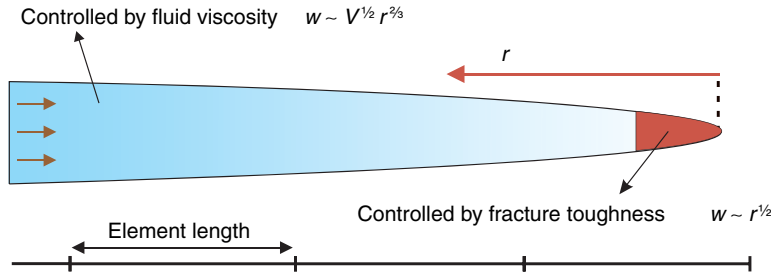


Fig. B-1—Multiscale tip behavior of a fluid-driven fracture.

In the part $r \ll l_{mk}$, the $w - r$ relation is $w \sim r^{1/2}$ and the tip-behavior solution is toughness-dominated,

$$w_k = \frac{K_I'}{E'} r^{\frac{1}{2}}. \quad \dots \dots \dots (B-2)$$

In the part $r \gg l_{mk}$, the $w - r$ relation is $w \sim V^{1/3} r^{2/3}$, and the tip-behavior solution is viscosity-dominated,

$$w_m = 2^{\frac{1}{3}} 3^{\frac{5}{6}} \left(\frac{\mu' V}{E'} \right)^{\frac{1}{3}} r^{\frac{2}{3}}. \quad \dots \dots \dots (B-3)$$

In most numerical models, the classic $w - r$ relation (Eq. B-2) is typically used as a propagation criterion for locating the tip position, which is only valid in a small area close to the fracture tip ($r \ll l_{mk}$) as mentioned. However, in many circumstances, the characteristic length l_{mk} is extremely small, and then very fine meshes are required to ensure that the computational length scale (e.g., element length) is much less than l_{mk} ; otherwise, the calculation will introduce unacceptable errors.

To solve this issue, instead of using the $w - r$ relation (Eq. B-2), we adopt a universal asymptotic solution (Dontsov and Peirce 2015) as the propagation criterion to update the fracture-tip position in the model,

$$\lim_{r \rightarrow 0} w = \left(\frac{K_I'^3}{E'^3} r^{\frac{3}{2}} + 2 \cdot 3^{\frac{5}{6}} \frac{\mu' V r^2}{E'} \right)^{\frac{1}{3}}. \quad \dots \dots \dots (B-4)$$

In numerical simulation, the V can be represented as

$$V = (r - r_o) / \Delta t, \quad \dots \dots \dots (B-5)$$

in which r and r_o are the distances from a specified point to the tip at the current timestep and last timestep. Thus, if we combine Eq. B-5 with Eq. B-4, we obtain

$$\lim_{r \rightarrow 0} w = \left[\frac{K_I'^3}{E'^3} r^{\frac{3}{2}} + 2 \cdot 3^{\frac{5}{6}} \frac{\mu' (r - r_o) r^2}{\Delta t E'} \right]^{\frac{1}{3}}. \quad \dots \dots \dots (B-6)$$

In Eq. B-6, when the fracture opening is given, r is the only unknown parameter. Then, Newton's method can be adopted to calculate r and to update the tip position. Compared with Eqs. B-2 and B-3, Eq. B-6 is a more universal $w - r$ relation representing the entire multiscale tip behavior, and it effectively captures the whole transition from $w \sim r^{1/2}$ to $w \sim V^{1/3} r^{2/3}$ (Dontsov and Peirce 2015). When using the propagation criterion (Eq. B-6), the limitation of the computational length scale in the fracture-tip zone is relaxed naturally for locating the fracture-tip position.

In multiple fluid-driven fracture growth, the preceding universal asymptotic solution (Eq. B-6) is modified further for mixed I/II Mode by adopting the maximum hoop-stress criterion (Erdogan and Sih 1963). By introducing the maximum hoop-stress criterion into Eq. B-6, the latter becomes Eq. 7 in the context.

Appendix C: Pressure Continuity in the Wellbore

In the problem mentioned in the Governing Equations subsection, the inlet flow rates into two fractures (or so-called fluid partitioning) q_1 and q_2 are unknown and undetermined at each timestep. The fluid partitioning is dynamically varied, and its value depends on the elasto-hydrodynamics coupling, fracture interaction, and wellbore conditions. To solve this fluid-partitioning problem, the mass balance and the pressure continuity in the wellbore should be used together.

In most of the multiple-fracture models (e.g., Bungler and Peirce 2014; Lecampion and Desroches 2015b; Wu and Olson 2015; Zeng et al. 2017), equations similar to the Kirchhoff circuit laws are typically applied to obtain the fluid partitioning, because the behavior of fluid flowing in the wellbore is analogous to the electricity flowing in the electrical-circuit network (Siriwardane and Layne 1991; Elbel et al. 1992). In each timestep, the fluid pressure should be continuous in the wellbore, and the total injection rate is equal to the sum of flow rates into each fracture. As shown in Fig. C-1, when considering the continuity of pressure in the fracturing stage (with N fractures) and calculating the fluid pressure at point O by accumulating pressure drops along different paths, we can find the relation as

$$p_1^{\text{pf}} + p_1^{\text{inlet}} = p_2^{\text{wf}} + p_2^{\text{pf}} + p_2^{\text{inlet}} = \dots = p_N^{\text{wf}} + p_N^{\text{pf}} + p_N^{\text{inlet}}, \quad \dots \dots \dots (C-1)$$

in which p_i^{wf} is the pressure drop caused by wellbore friction from the first fracture inlet to the i th fracture inlet, and p_i^{pf} is the pressure drop caused by perforation friction at the i th fracture inlet. The i th-fracture-inlet fluid pressure p_i^{inlet} , associated with the elasto-hydrodynamics mechanism and fracture propagation and interaction, can be obtained by solving the elasto-hydrodynamics equations mentioned in Appendix A.

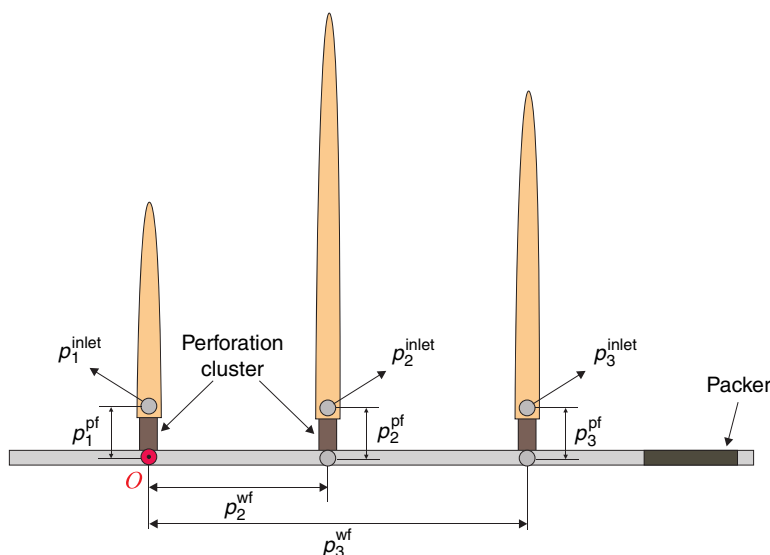


Fig. C-1—Schematic for the continuity of pressure in the wellbore ($N = 3$ fractures).

In multistage hydraulic fracturing, the pressure drop p_i^{wf} caused by wellbore friction can be estimated from flow rates, wellbore, and fluid viscosity (Valk and Economides 1995). In the early stage of hydraulic fracturing, this pressure drop p_i^{wf} between fractures (within a fracturing stage) is much less than fluid pressure p_i^{inlet} and relatively negligible. Another pressure drop p_i^{pf} caused by perforation friction can be estimated from flow rates, perforation number, perforation diameter, and fracturing-fluid density, as presented in Crump and Conway (1988). For some numerical studies related to the pressure drop p_i^{pf} , refer to Wu et al. (2017) and Lecampion and Desroches (2015b). Recalling the pertinent assumption in the Assumptions subsection, a negligible p_i^{pf} is adopted in this numerical study. Then letting $N = 2$ and considering the mass balance together, Eq. C-1 becomes

$$\begin{cases} Q = \sum_{i=1}^{N=2} q_i \\ p_1^{\text{inlet}} = p_2^{\text{inlet}} \end{cases} \quad \dots \dots \dots (C-2)$$

The inlet-fluid pressure p_i^{inlet} can be considered as a function of q_i . In each timestep, trial solutions for q_i are set first for subsequently solving the elasto-hydrodynamics coupling. Then, the Newton-Raphson iteration method is adopted to find the fluid partitioning q_i and the inlet-fluid pressure p_i^{inlet} by minimizing the residual ϵ ,

$$\|p_1^{\text{inlet}} - p_2^{\text{inlet}}\| = \epsilon. \quad \dots \dots \dots (C-3)$$

Xiyu Chen is PhD degree candidate in petroleum engineering at Southwest Petroleum University, China. His main interest is the numerical simulation of hydraulic-fracture growth and promotion of multiple-fracture simultaneous growth. Chen earned a BS degree from Southwest Petroleum University. He is a member of SPE.

Jinzhou Zhao is the president of and a professor at Southwest Petroleum University. His main interest is the promotion of unconventional-hydrocarbon recovery. Zhao earned an MS degree from Southwest Petroleum University.

Wenyi Yan is a professor in mechanical and aerospace engineering at Monash University. His main interest is applied mechanics of solids and structures, composite structures, fractures, and fatigue of materials. Yan earned a PhD degree from Tsinghua University.

Xi Zhang is a research scientist at CSIRO Energy. His main interest is in solving geomechanics problems with numerical methods. Zhang earned a PhD degree in mechanical engineering from the University of Sydney. He is a member of SPE.